Dalton Transactions

PAPER

View Article Online
View Journal | View Issue

Cite this: *Dalton Trans.*, 2014, **43**, 17034

Time-resolved and photoluminescence spectroscopy of θ-Al_2O_3 nanowires for promising fast optical sensor applications†

Jitendra Gangwar,[a,b] Bipin Kumar Gupta,[a] Pawan Kumar,[a] Surya Kant Tripathi[b] and Avanish Kumar Srivastava*[a]

Received 19th June 2014,
Accepted 18th September 2014

DOI: 10.1039/c4dt01831a

www.rsc.org/dalton

Herein, we have demonstrated the high yield facile growth of Al_2O_3 nanowires of uniform morphology with different polymorph phases (*e.g.* γ, δ and θ) *via* a hydrothermal method with varying calcination temperatures. The synthesized θ-Al_2O_3 nanowires were well characterized by XRD, FTIR, SEM/EDAX, AFM and HRTEM techniques. Microstructural analysis confirmed that the dimensions of the individual θ-Al_2O_3 nanowires are approximately in the ranges 5–20 nm in width and 40–150 nm in length, and the aspect ratio is up to 20. AFM results evidenced the uniform distribution of the nanowires with controlled morphology. Furthermore, UV-vis spectroscopic data reveal that the estimated optical band gap of the θ-Al_2O_3 nanowires was ~5.16 eV. The photoluminescence spectrum exhibits blue emission upon excitation at a wavelength of 252 nm. Time-resolved spectroscopy demonstrates that these nanowires illustrate a decay time of ~2.23 nanoseconds. The obtained photoluminescence results with a decay time of nanoseconds suggest that the θ-Al_2O_3 phase could be an exceptional choice for next generation fast optical sensors.

1. Introduction

Recent thrusts in luminescent nanomaterials research of all kinds of possible crystalline oxide nanostructures have largely been attributed to their multifunctional properties and huge applications in many areas such as display technology, sensor technology, optoelectronic devices, bio-imaging and many others.[1–7] The current challenge in this area is to develop high yield efficient luminescent materials with controlled morphologies and desirable properties. Although in the last few decades, many semiconductor luminescent materials have already been proven to have good performance in optical display and sensor applications.[8–10] Besides the commercial success of these semiconducting oxide materials, there has been rapidly growing interest in large band gap crystalline oxides, such as BeO, CaO, SrO, MgO, BaO, ZrO_2, Al_2O_3, B_2O_3 and La_2O_3, because of their novel properties and multiple functionalities.[11–15] To the best of our knowledge, among all the above mentioned oxides, Al_2O_3 nanostructures exhibit excellent luminescence properties as well as decay times of nanoseconds, which are required for many optoelectronic devices and optical sensors.[16–18]

It is well established that the potential applications of Al_2O_3 (aluminium oxide, alumina) have been reported in many renowned areas such as abrasives, electrical insulators, electronic substrates, adsorbents, and inexpensive catalysts. The advantages of this oxide nanostructure are due to its facile synthesis route, by which we can produce this material in large quantities with a controlled morphology.[19–25] There are several transition polymorph phases (*e.g.* γ, δ, η, σ, θ, κ, β, *etc.*) in Al_2O_3 nanostructures.[26–29] It is difficult to customize the method for the synthesis of isolated γ, δ, η, θ, κ and β phases. These metastable transition alumina phases, including the γ, δ and η phases, possess face centered cubic packing of the oxygen anions, but the unique feature of the θ-Al_2O_3 is that aluminium cations (Al^{3+}) are equally distributed between the tetrahedral and octahedral sites in the oxygen lattice. Although metastable, θ-Al_2O_3 is a very stable and well-known structure with a monoclinic symmetry, and preserves its structural identity even at temperatures up to 1300 K, which generates new chemistry for the understanding of the θ-Al_2O_3 phase.[30–32] The luminescent properties of these nanostructures are extremely important because of their large band gaps (~8.8 eV) as well as many other interesting properties such as tunable electronic band gaps, high thermal stability and lattice dynamics of the

[a]*National Physical Laboratory, Council of Scientific and Industrial Research, Dr. K. S. Krishnan Road, New Delhi, 110012, India*
[b]*Department of Physics, Panjab University, Chandigarh, 160014, India.*
E-mail: aks@nplindia.org, avanish.aks555@gmail.com; Fax: +(91)11 45609310; Tel: +(91)11 45609308

† Electronic supplementary information (ESI) available. See DOI: 10.1039/c4dt01831a

individual phases of the alumina.[33–42] The properties of these nanostructures can be easily explored as well as understood, which creates enormous interest among various research groups working in this area. Currently, the synthesis of low-dimensional (one-dimensional, 1-D) luminescent nanomaterials with different morphologies, such as nanowires, tubes, belts, pillars and rods, has evolved due to their large aspect ratio and high luminescence efficiency as well as their relevant potential uses in nano-optics, sensors and logic gates.[43–52] However, few attempts have been made to synthesize AlO(OH) nanowires, due to their lower stability and the hygroscopic nature of AlO(OH), which limit its applications in optical displays. In this area, Al_2O_3 nanowires have been proposed to overcome such problems.[53,54] Besides the different morphogeneses and methodologies used for the synthesis of Al_2O_3 nanostructures, nanowires of Al_2O_3 with a single phase, either the γ-, δ- or κ-phase, have been well established and explored in detail.[53–55] Among all of the phases of Al_2O_3 nanostructures, the γ-Al_2O_3 and θ-Al_2O_3 phases are important for their potential applications in optoelectronic devices as well as in optical sensors due to their newly emerging defect induced luminescent properties. The advantages of the θ-phase over the γ-Al_2O_3 are its larger grain size and the smaller number of defects in its crystalline structure that can help to tune the optical properties to the desired applications. Simultaneously, the probability of producing the pure θ-phase is quite difficult and has not been explored much by any research groups. Only one effort has been done till date to produce stable θ-Al_2O_3 by introducing chromium (Cr) as the catalyst. However, a theoretical explanation has been well established by Lodziana *et al.* using DFT theory.[30] To the best of our knowledge, the optical properties of θ-Al_2O_3 are not yet reported to date. Here, we focus on exploring, with time-resolved spectroscopy, the luminescent properties of the alumina θ-phase at room temperature, including comparative studies with the γ- and δ-phase, which have been not reported to date to the best of our knowledge; that is the focal point of our present investigations.

It is interesting to note that various crystalline oxide nanostructures such as Al_2O_3, MgO, and ZnO demonstrate a broad photoluminescence (PL) spectrum with blue emission as well as an emission decay time in the nanosecond regime. The luminescence properties of oxide nanostructures are well established and are caused by the existence of external/internal defects or color centers, or by external impurities.[55–62] However, the emission of strong tunable blue PL is closely related to that of the oxygen vacancy and its electronic states.

In the present investigation, we employed a facile hydrothermal process to synthesize high-yield Al_2O_3 nanowires with a uniform, controlled morphology, which can be easily produced in large quantities at an economic cost. Furthermore, a plausible mechanism for the synthesis of the nanowires has been proposed, which is based on systematic gross structural analysis. Moreover, an extensive morphogenesis study on the optical properties of these nanowires was examined in detail and was correlated with electron micrographs obtained for θ-Al_2O_3 nanowires. Finally, time-resolved spectroscopic analysis was used to investigate the Al_2O_3 nanowires at different emission wavelengths of 397, 418, 467 and 560 nm with a fixed excitation wavelength of 375 nm for promising fast optical sensor applications.

2. Experimental

2.1. Materials

Aluminium chloride hexahydrate laboratory reagent ($AlCl_3{\cdot}6H_2O$, 97%, Qualikems Pvt Ltd), ammonia solution (NH_4OH, 25%, Rankem) and NaOH were used as received without any further purification. Millipore water (18 MΩ) was used as the solvent and the reaction medium in all the synthesis endeavours. Absolute ethanol (99.9%, AR) was used for further purification and other characterizations.

2.2. Synthesis

The synthesis process is simple and effective, and creates a new kind of chemistry for the stable θ-Al_2O_3 phase in large quantities. Basically, this process involves two steps: (i) formation of the AlO(OH) nanostructures; (ii) conversion of AlO(OH) to γ-, δ- and θ-Al_2O_3.

2.2.1. Synthesis of the AlO(OH) nanostructures. The 1-D boehmite nanowire (AlO(OH)) was fabricated using $AlCl_3{\cdot}6H_2O$ as the alumina precursor by a facile hydrothermal method. In a typical synthesis process, 1.0 M of $AlCl_3{\cdot}6H_2O$ was dissolved in 50 ml of Millipore water to produce transparent $AlCl_3$. A 1.0 M aqueous solution of NaOH in 25 ml of Millipore water was mixed into the above solution. An appropriate amount of NH_4OH solution was added to this solution dropwise under constant stirring at room temperature. This procedure was carried out until the pH of the solution reached 6.0 and a dense white coloured precipitate appeared, signifying the formation of $Al(OH)_3$. The solution was stirred vigorously for a further 30 min and then sealed in a Teflon-lined stainless steel autoclave of 100 ml capacity, and heated at 200 °C for 24 h. After naturally cooling to room temperature, the solid product was collected by filtration and washed with Millipore water and ethanol several times. The solid was finally dried at 60 °C for 12 h and a white powder product was obtained, indicating the formation of AlO(OH) which is later referred to as the uncalcined sample (C_0).

2.2.2. Synthesis of γ-, δ- and θ-Al_2O_3. The nanowires of Al_2O_3 were fabricated by the calcination of the uncalcined sample. The uncalcined sample was calcined at three different temperatures, 500, 800 and 1000 °C, in air with a heating rate of 3 °C min^{-1} for 2 h in a muffle furnace under static conditions. These obtained products are later referred to as the calcined samples, C_1, C_2 and C_3 for calcination temperatures of 500, 800 and 1000 °C, respectively.

The plausible chemical reactions that lead to the formation of alumina are given below:

$$AlCl_3{\cdot}6H_2O \rightarrow AlCl_3 + 3H_2O \rightarrow Al(OH)_3 + 3HCl$$

$$Al(OH)_3 \rightarrow AlO(OH) + H_2O$$

$$AlO(OH) \rightarrow Al_2O_3 + H_2O$$

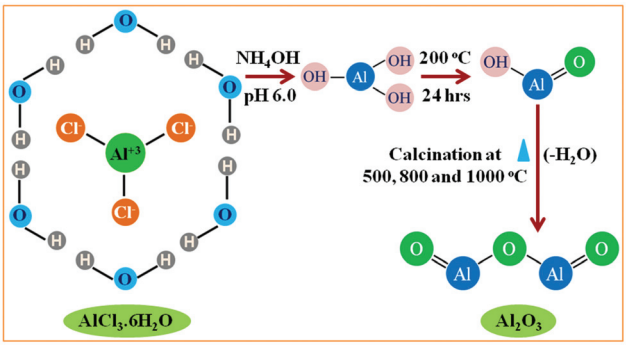

Scheme 1 The plausible structural model for the synthesis of the Al_2O_3 nanowires.

The general stoichiometric formulae of the Al_2O_3 nanowires of different phases are described and can be obtained by varying the calcination temperature in the following sequence:

$$AlO(OH) \rightarrow \gamma - Al_2O_3 \rightarrow \delta - Al_2O_3 \rightarrow \theta - Al_2O_3$$

The plausible structural model for the synthesis of the γ-, δ- and θ-Al_2O_3 nanowires and the systematic phase transformation *via* an increase in temperature has been demonstrated in Schemes 1 and 2, respectively.

2.3. Characterization

Crystallographic characteristics of the prepared samples were recorded on a Rigaku benchtop X-ray diffractometer using monochromatic Cu-$K_{\alpha 1}$ radiation (λ = 1.5406 Å). FTIR spectra were recorded with a single beam Perkin Elmer (Spectrum BX-500) spectrometer. Surface morphology and elemental analyses of the samples were conducted by a scanning electron microscope (Zeiss EVO MA-10 SEM operating at 10 keV) equipped with an energy dispersive spectrometer (EDS; OXFORD INCA ENERGY 250). The surface topography was recorded with an atomic force microscope (AFM; Multimode V, Veeco Instruments; now Bruker AXS) operating in tapping mode. High-resolution transmission electron microscopy analysis and fast Fourier transformation (FFT) patterns were recorded on a HRTEM (FEI Tecnai G2 F30 STWIN at 300 keV). UV-vis spectra of all the samples were investigated by a UV-vis spectrometer (UV-2401 PC, Shimadzu Corporation Japan). Room temperature photoluminescence (PL) investigations were performed using a fluorescence spectrometer (Edinburgh Instruments, model FLSP-900) with a xenon lamp as the excitation source. Time-resolved PL (TRPL) was recorded using a time-correlated single-photon counting technique with a picosecond diode laser (375 nm) as the excitation source.

3. Results and discussion

Gross structural analysis of the uncalcined and calcined samples has been performed using XRD as shown in Fig. 1a. The XRD pattern of the uncalcined product is exhibited in the lower segment (Fig. 1a) and indicates the mixed phase of Al $(OH)_3$ and AlO(OH). The uncalcined sample consisted mainly of crystalline AlO(OH) with an orthorhombic crystal system (JCPDS 83-2384) and lattice constants of a = 0.369, b = 1.221 and c = 0.286 nm. The uncalcined product was further calcined at 500 °C for 2 h. The identified peak positions and the relative intensities of the peaks (Fig. 1a) correspond to the cubic crystal system of γ-Al_2O_3 with a lattice constant of a = 0.792 nm (JCPDS 29-0063). No diffraction peaks were observed for the characteristic peaks of the AlO(OH) and other impurities, which indicates the complete transformation to the γ-Al_2O_3 phase. With a further increase of the temperature up to 800 °C, the γ-Al_2O_3 phase transforms into δ-Al_2O_3, as shown in Fig. 1a. The observed XRD data confirms that the δ-Al_2O_3

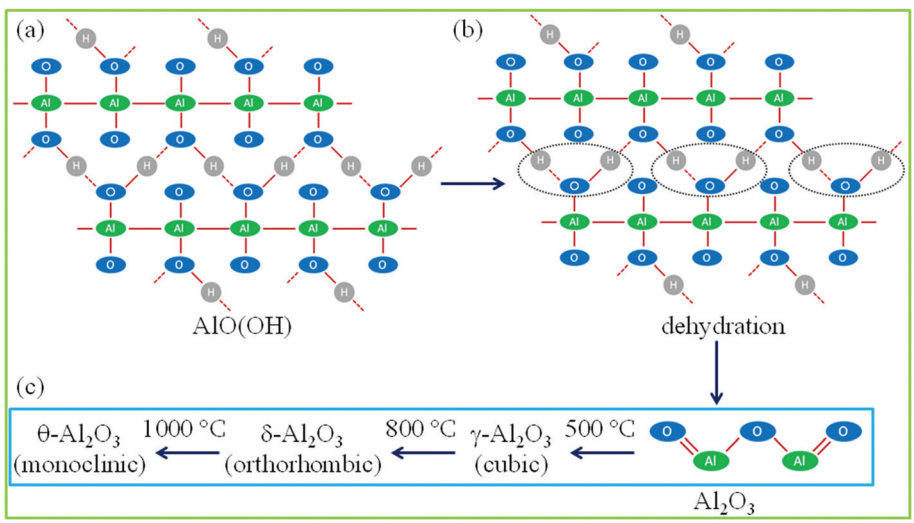

Scheme 2 Schematic depiction of the AlO(OH) → Al_2O_3 transformation process; (a) isolated AlO(OH) molecules becoming aligned, (b) the loss of the water molecules (the dehydration process), (c) the transformation sequence of Al_2O_3 with different polymorphs at increasing calcination temperatures.

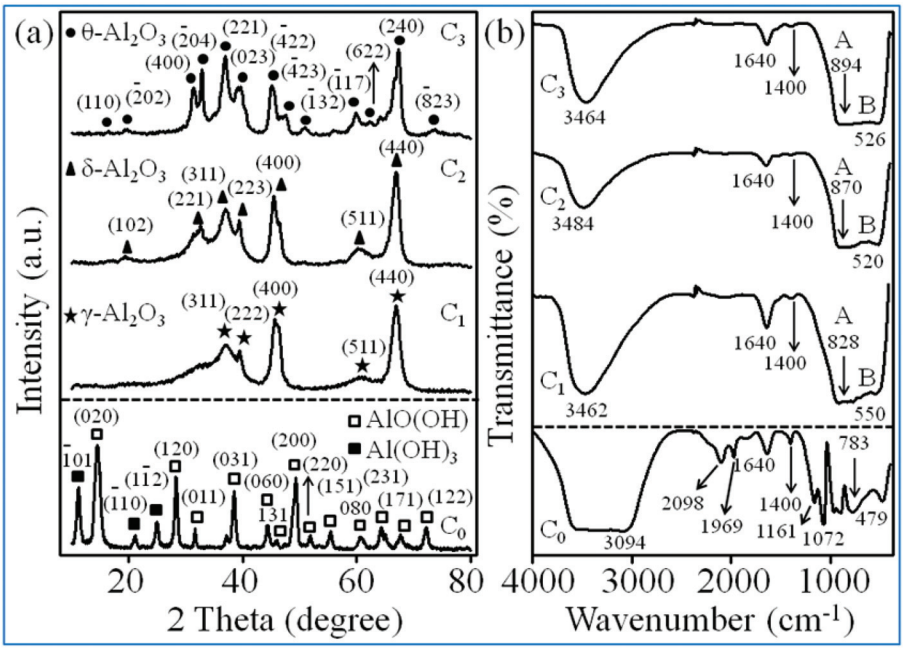

Fig. 1 (a) XRD patterns and (b) FTIR spectra of the as-synthesized AlO(OH) nanowires (C_0) and the Al_2O_3 nanowires calcined at three different temperatures: (C_1) 500 °C, (C_2) 800 °C and (C_3) 1000 °C.

phase was an orthorhombic crystal system with cell parameters of a = 0.793, b = 0.795 and c = 1.171 nm (JCPDS 46-1215). On further increasing the temperature up to 1000 °C, several other diffraction peaks occurred, which correspond to the θ-Al_2O_3 phase (Fig. 1a). The XRD pattern of the calcined sample at 1000 °C evidenced the θ-Al_2O_3 phase with a monoclinic crystal system having lattice parameters of a = 1.174 nm, b = 0.572 nm and c = 1.124 nm; β = 103.34° (JCPDS 11-0517). No peaks corresponding to impurities or remnants of $AlCl_3$ were detected, which indicated the complete transformation of δ-Al_2O_3 into θ-Al_2O_3.

For more clarity, comparative studies between all three phases of Al_2O_3 and standard JCPDS cards are shown in Fig. S1.† We have also estimated the crystallite sizes of the different phases of Al_2O_3 using the Debye–Scherrer equation. The estimated crystallite sizes were obtained from the FWHMs of the XRD patterns for the different crystalline phases as shown in Fig. 1a. The estimated crystallite size for γ-, δ- and θ-Al_2O_3 are within the range 7–21 nm for the uncalcined product, while the crystallite sizes of the calcined product at the different temperatures, 500, 800 and 1000 °C, were 3–7, 4–65 and 4–86 nm, respectively. The XRD results reveal that the transformation of the different phases usually occurs due to the removal of water molecules from two AlO(OH) octahedrons with the help of internal condensation of a proton and a hydroxyl ion. The remaining oxygen ion serves as a link between two Al atoms. The structural changes with respect to the calcination temperature can be easily realized *via* the unit cell model as shown in Scheme 3.

The phase transformations were further confirmed by FTIR spectroscopy. Fig. 1b exhibits the FTIR spectra of the nanowires of boehmite AlO(OH) and the different phases of Al_2O_3. It is observed that the FTIR absorption spectrum for the AlO(OH) nanowires illustrates two broad bands at 3289 and 3094 cm^{-1}, which are attributed to asymmetric and symmetric vibrations in the OH groups. Two intense bands were observed at 2098 and 1969 cm^{-1} for the AlO(OH) nanowires, indicating the combination bands. The other four absorption bands (1161, 1072, 783 and 479 cm^{-1}) appeared in the region 400–1200 cm^{-1} as shown in Fig. 1b. The small shoulder at 1161 cm^{-1} is assigned to O–H bending. The strong and sharp absorption band at 1072 cm^{-1} is attributed to the (OH)–Al═O asymmetric stretching vibration. The absorption bands at 783 and 479 cm^{-1} correspond to, respectively, (AlO)–O–H angle bending and O═Al–(OH) angle deformation (wagging). For the calcined products of Al_2O_3, aluminium can coordinate differently with oxygen. A tetrahedral coordination (AlO_4) is expected to provide the Al–O stretching modes in the region 750–850 cm^{-1}, whereas in an octahedral coordination (AlO_6), the Al–O stretching modes are expected in the region 500–750 cm^{-1}.

However, the absorption band A is blue-shifted from 828 (γ-Al_2O_3) to 870 (δ-Al_2O_3) and 894 (θ-Al_2O_3) cm^{-1}; and the band B is first red-shifted from 550 (γ-Al_2O_3) to 520 cm^{-1} (δ-Al_2O_3), and further blue-shifted to 526 cm^{-1} (θ-Al_2O_3). The blue-shifts are occurred due to the size-confinement effect, while the red-shifts are originated from dangling bonds present on the surface of nanostructures. The broadening of the modes is probably ascribed to the transformation of the hydrate into an oxide and confirms the conversion from AlO(OH) to Al_2O_3.

The absorption bands at around 1640 cm^{-1} for both the uncalcined and calcined products are the well-known H–O–H

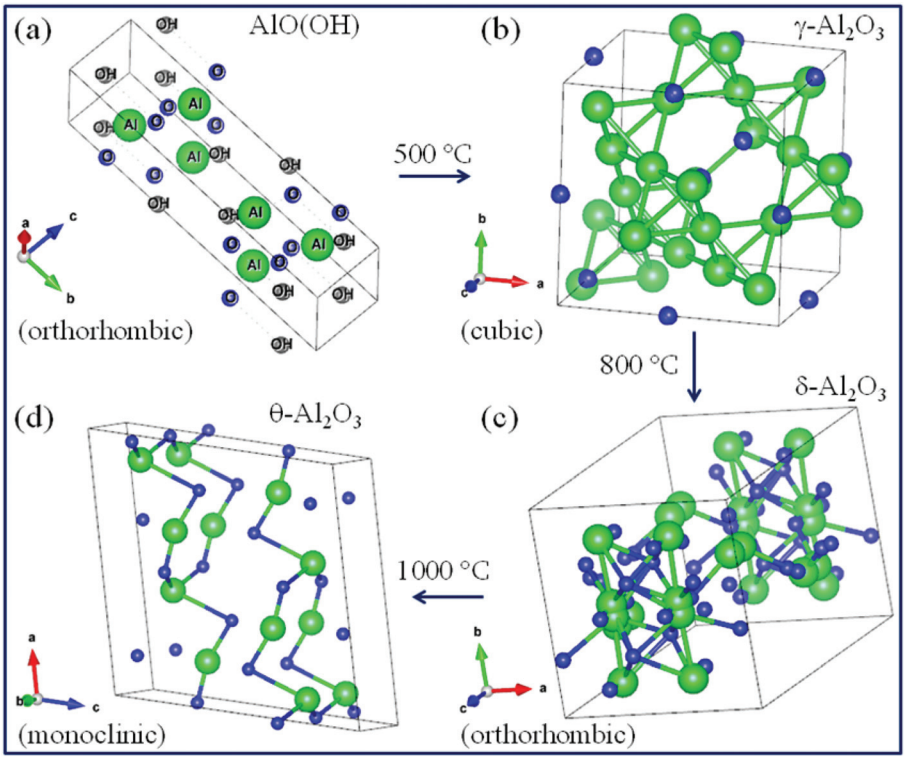

Scheme 3 Unit cells of (a) uncalcined AlO(OH) (orthorhombic) and calcined Al_2O_3: (b) γ-Al_2O_3 (cubic), (c) δ-Al_2O_3 (orthorhombic) and (d) θ-Al_2O_3 (monoclinic). The aluminium and oxygen atoms are shown by the light and dark spheres (green and blue in color), respectively.

angle bending vibration band of weakly bound molecular water. As a comparison, the intensity of this band is stronger for the AlO(OH) nanowires as more H_2O molecules are associated in the crystal. The absorption bands appearing at about 1400 cm^{-1} for the products are assigned to the presence of carbon–hydrogen (CH_3), –carbon (C–C) and –oxygen (C═O) deformations. The intensities of both these vibrational modes disappear as we shift from the uncalcined product to the Al_2O_3 products, indicating the removal of the surface adsorbents (H_2O, CO_3^{2-}) with increasing calcination temperatures.

The surface morphology and microstructural characterizations of the different phases were confirmed through scanning electron microscopy as well as high resolution transmission electron microscopy. In all phases, the morphologies of the samples appeared to be nanowire like structures. Here we only demonstrate the morphology of the final product (calcined at 1000 °C). Fig. 2a depicts the scanning electron microscopy (SEM) image of the θ-Al_2O_3 nanowires obtained by the calcination of the corresponding precursors at 1000 °C. A typical SEM micrograph (inset in Fig. 1a) indicates that the length is within the range 450–900 nm and the average diameter of the products is approximately 60 nm. The EDS analysis (Fig. 2b) reveals the weight content of Al and O to be 47.15% and 52.85%, respectively, giving an atomic content ratio Al/O of 34.60/65.40, which verifies the formation of the alumina particles to a large extent, since no other element was detected. HRTEM was performed to evaluate the detailed microstructural characterization, size and atomic scale imaging of the θ-Al_2O_3 nanowires, corresponding to a calcination temperature of 1000 °C, and the results obtained are illustrated in Fig. 2c–e. A bright-field TEM image of the sample at a high magnification shows that the sample consists of a large quantity of nanowires with almost uniform morphology and clearly indicates that the target alumina product exhibits a 1D nanostructure of regular nanowires. Fig. 2c reveals the low magnification image of the alumina nanowires. They are approximately 5–17 nm in width and 40–150 nm in length, which shows full consistency with the observed SEM results. The aspect ratio of the θ-Al_2O_3 nanowires was up to 20. The HRTEM image (Fig. 2d) indicates that the prepared alumina nanowires exhibit clear lattice fringes with an estimated interspacing of 0.20 nm that reflects the $(\bar{4}22)$ plane of θ-Al_2O_3; correspondingly the FFT pattern is also shown in Fig. 2e. The results reveal that the $(\bar{4}22)$ plane shows good consistency with the observed XRD patterns. The topographical morphology and homogeneity of the nanowires has been characterized by atomic force microscopy in the tapping mode as shown in Fig. 2f. The AFM image exhibits a homogenous distribution of the nanowires with an average length of about 300 nm and diameters in the range 30–50 nm. The AFM image also reveals the efficiency of the hydrothermal process for high-yield preparation of these θ-Al_2O_3 nanowires in the present investigation.

Optical properties and related defect states have been investigated by UV-vis and photoluminescence (PL) spectroscopy, respectively and the results are displayed in Fig. 3. Fig. 3a

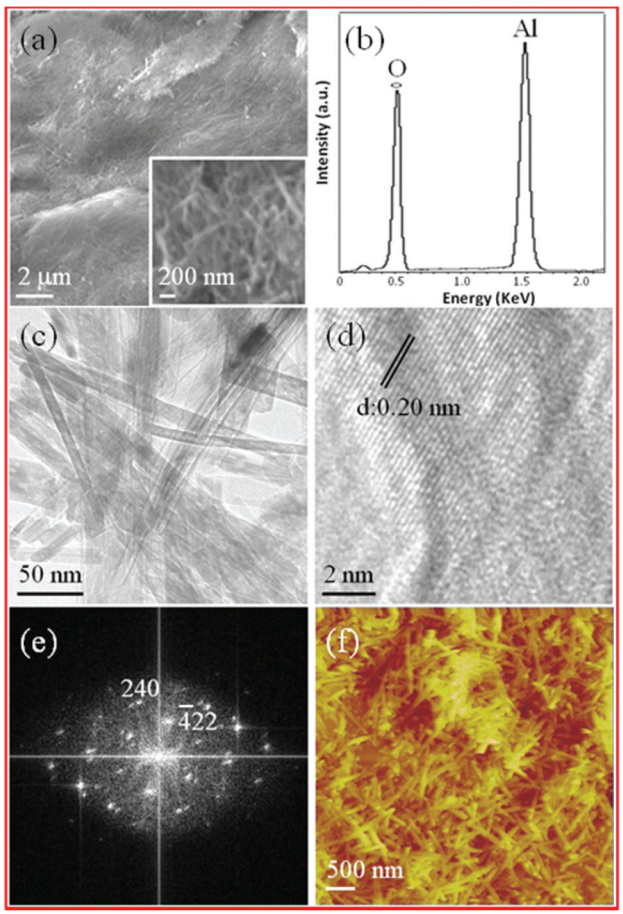

Fig. 2 (a) SEM image, (b) EDAX spectrum, (c) bright-field low magnification TEM micrograph, (d) HRTEM images showing the lattice fringe scaling, (e) FFT pattern and (f) AFM image of the Al_2O_3 nanowires synthesized at 1000 °C. The inset of (a) provides the high-magnification image of the corresponding sample.

demonstrates the UV-vis properties of the nanowires calcined at different temperatures.

The obtained UV-vis spectra reveal that the calcined sample has an absorption band at around 208 nm (5.96 eV) due to the $O^{2-} \rightarrow Al^{3+}$ charge transfer transitions. The presence of the absorption band is attributed in terms of adsorbed water species and this interaction with other water molecules through hydrogen bonding. The other two peaks at 271 (4.57 eV) and 274 nm (4.52 eV) were obtained for the samples calcined at 500 and 800 °C, respectively, which indicate that the adsorption sites are different. The optical band gaps of the nanowire have been estimated from the absorption spectrum as shown in Fig. 3b. The optical band gaps have been determined from the UV-vis spectra utilising the Tauc equation:

$$(\alpha h\nu)^n = (h\nu - E_g) \quad (1)$$

where α = absorption coefficient, $h\nu$ = energy of the incident photon, B = a constant characteristic of the material, n = 2 for direct band gap transition or $\frac{1}{2}$ for indirect band gap transition, and E_g = optical band gap of the sample.

The intercept on the abscissa of the plot $(\alpha h\nu)^2$ *vs.* $h\nu$ provides the band gap energy of the samples (Fig. 3b). The corresponding band gap energy for the θ-Al_2O_3 nanowires was determined to be 5.16 eV, which is very close to the theoretical estimated band gap of the θ-Al_2O_3 phase.[27]

Photoluminescence is an important tool for exploring the electronic energy band structure and surface defect analysis of a material. Generally the luminescence phenomenon occurring in any material is due to its intrinsic behavior (band edge structure) and other internal or external factors like intrinsic or extrinsic defect states. In the present investigation, we observed a broad emission spectrum of the calcined products at 1000 °C ranging from 360 to 600 nm (2.07–3.44 eV) at an excitation wavelength of 252 nm (4.92 eV) as shown in Fig. 3c. In this regime, we obtained two broad peaks of blue emission at 397 and 418 nm (3.12 and 2.96 eV) and one peak of green emission at about 560 nm (2.21 eV), one sharp blue emission at 467 nm (2.66 eV), together with three weak shoulders of blue emission at 435, 481 and 490 nm (2.85, 2.58 and 2.53 eV). The major intense blue emission peak at 397 nm, with colour coordinates x = 0.1845 and y = 0.1711 for PL excitation at 252 nm (4.92 eV) (as shown in Fig. 3d), may be attributed to the cationic vacancies of Al^{3+}.[6,12,58] The peaks observed at 397 and 418 nm originated from F^+ (oxygen vacancies with one electron) and F centers, respectively.[1,6,11,40,58,59] The blue and green emissions at about 490 and 560 nm were closely associated with F_2 and F_2^{2+} centers.[60] We have also elucidated the corresponding energy levels on the basis of the obtained excitation and emission spectra as shown in Fig. 4a.

In order to investigate the dynamic nature of the photoluminescence, a time-resolved PL measurement was performed. The luminescence decay time is mainly determined by the concentration of defects associated in the nanostructure which trap the electrons and/or holes and hinder their recombination process. Time-resolved PL spectroscopy was carried out on the θ-alumina nanowires and the decay profile is displayed in Fig. 4b and 4c. The room temperature PL decay profile at 397 nm (3.12 eV) emission with 375 nm excitation wavelength using a picosecond diode laser exhibits the decay time to be within the range 0–40 ns. Double-exponential fits were used to determine the decay time of the θ-Al_2O_3 nanowires. The decay time data was best fitted to a double-exponential function, characterized by two decay time constants τ_1 and τ_2:

$$I(t) = A_1\exp(-t/\tau_1) + A_2\exp(-t/\tau_2) \quad (2)$$

where A_i is the PL intensity of the i_{th} component at t = 0.

The parameters obtained from the exponential fitting are shown in Fig. 4c. The obtained decay components, τ_1 = 0.26 ns and τ_2 = 2.39 ns, show that two kinds of recombinations occur during the luminescence phenomenon; a fast and a slow process. The two different kinds of decay components occur due to the different defect states that exist between the conduction band and the valence band of the θ-Al_2O_3 nanowire structures. The ratio of fast to slow decay components is about

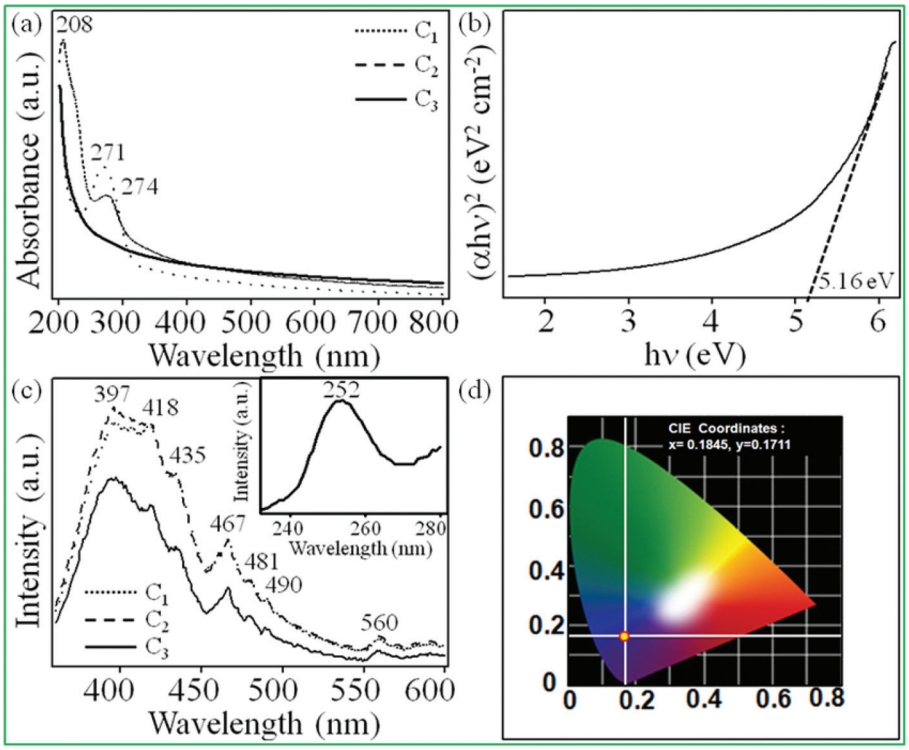

Fig. 3 (a) UV-vis spectra of the aqueous dispersion of the Al_2O_3 nanowires calcined at (C_1) 500, (C_2) 800 and (C_3) 1000 °C. (b) The Tauc plots for the Al_2O_3 nanowires obtained by calcination at 1000 °C. (c) Room temperature photoluminescence spectra of the calcined Al_2O_3 samples recorded upon excitation at 252 nm, showing intense blue emission. The inset illustrates the photoluminescence excitation spectrum of the θ-Al_2O_3 nanowires obtained at 397 nm emission. (d) The color coordinates of the major emission peak of the θ-Al_2O_3 nanowires.

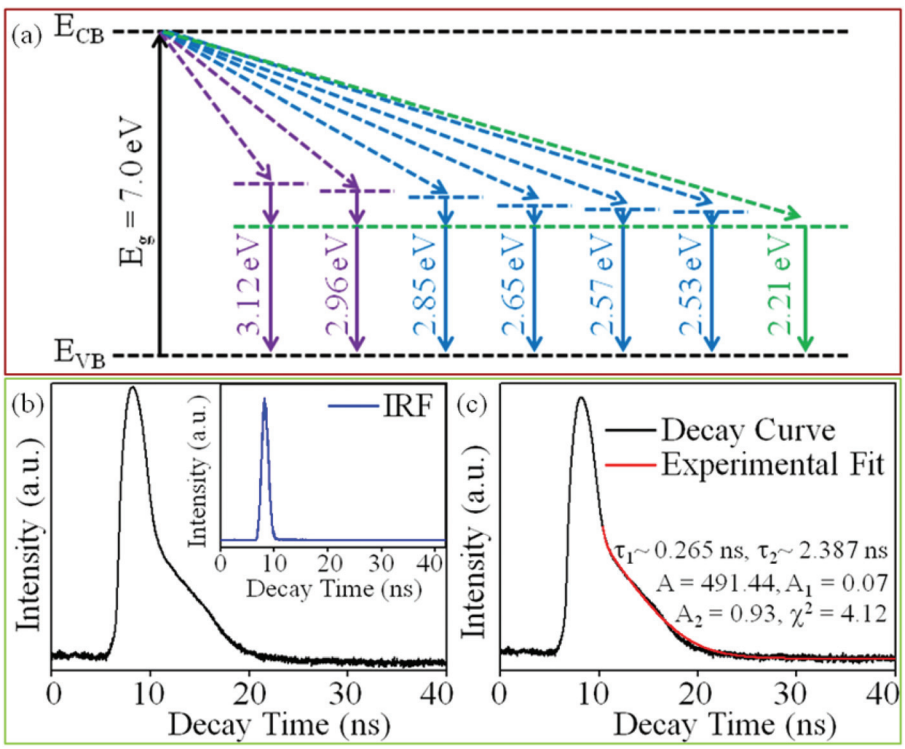

Fig. 4 (a) Energy level illustration on the basis of the obtained excitation and emission PL spectra of the θ-Al_2O_3 nanowires. (b) Time-resolved PL decay profile of the θ-Al_2O_3 nanowires recorded at room temperature and at 397 nm emission with a laser diode of 375 nm excitation wavelength; the inset presents the IRF spectrum. (c) The lifetime data and the parameters generated by exponential fitting.

nine, which reflects that the energy transfer process involves different kinds of defect states. However, it is difficult to explain the exact cause of the different decay components which are related to the recombination process, and there is no direct evidence for the correlation between the defect induced transitions and the decay dynamics. But it may be correlated to the monoclinic crystal structure of the θ-Al_2O_3 nanowires. We also performed time-resolved PL spectroscopy for the other two phases (γ- and δ-phase) including the θ-phase of Al_2O_3 with exponential fits as shown in the ESI, Fig. S2(a–b).† We obtained TRPL results of all three samples (C1, C2 and C3) and found that the decay time decreases from the γ-phase to the θ-phase of the Al_2O_3 nanowires, which was expected as shown in Table S1.† The TRPL results have a good correlation with the obtained PL results. The decay time is decreased because the defects are suppressed during the transfer from the γ-phase to θ-phase, and as a result, both PL intensity as well as decay TRPL decreased.

However, we tried to explore the different transitions relating to the defect sites but we could not see clear defect site energies, which distinguish all the kinds of transitions associated with the PL phenomenon, as shown in Fig. S3(a–b).† The results reveal that the decay profiles at different emission wavelengths of 397, 418, 467 and 560 nm demonstrate almost the same kind of decay characteristics except for decay times. It may be concluded that in all cases the transition occurs due to the combined effects of several types of defects induced in the θ-Al_2O_3 nanowires. No clear evidence has been found from the decay profiles which can be explored in the individual defect states. For more clarity, we have obtained exponential fit spectra and their generated decay times as shown in Table S2.† The TRPL results at different emission wavelengths of 397, 418, 467 and 560 nm at a fixed excitation wavelength of 375 nm are in good agreement with the obtained PL results, which was excepted.

However, we propose a plausible mechanism for the efficient energy transfer in the θ-Al_2O_3 nanowires, which is responsible for the defects induced in the photoluminescence phenomenon. Fig. 5 exhibits the ball-and-stick structure of the θ-Al_2O_3 nanowires, in which it can easily be seen that oxygen has three different crystallographic sites, among which the crystallographic sites O2 and O3 are equally responsible for the energy transfer (and have almost equal bond lengths) during the defect induced luminescence process. The O1 related defect state has different characteristics to the two mentioned above for the energy transfer. It may cause two kinds of components to exist in the present luminescence process.

For the double-exponential decay, the average decay time (τ_{av}) is determined by the following equation:

$$\tau_{av} = \frac{A_1\tau_1^2 + A_2\tau_2^2}{A_1\tau_1 + A_2\tau_2} \quad (3)$$

The average PL decay time for the θ-Al_2O_3 nanowires is calculated to be $\tau_{av} \sim 2.23$ ns and is highly suitable for fast optical sensing/switching applications. It is well-known that optical switches or optical sensors require the decay time to be in the nanosecond to picosecond range, which legitimates our TRPL spectroscopic results.[63]

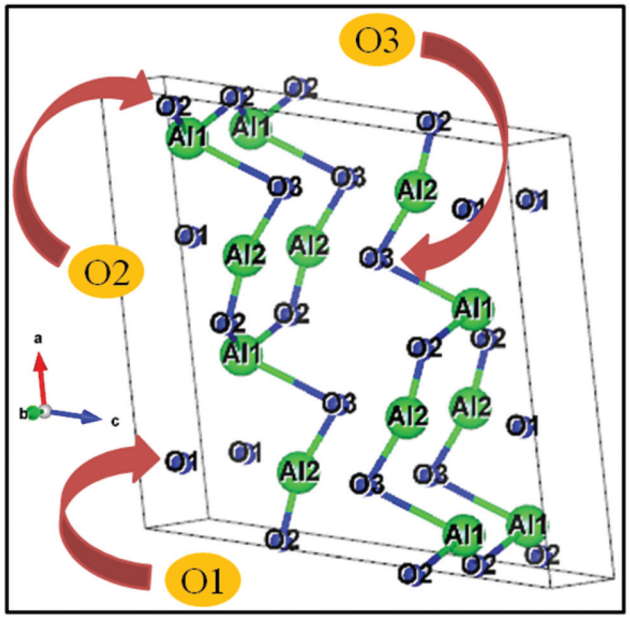

Fig. 5 Crystallographic sites for aluminium (Al) and oxygen (O) atoms in the unit cell of the θ-Al_2O_3 nanowires.

4. Conclusions

We have successfully synthesized Al_2O_3 nanowires with a controlled morphology in different phases by a facile hydrothermal process. This adopted route for the synthesis of θ-Al_2O_3 is very simple and effective, which creates new physical insights for obtaining large scale stable θ-Al_2O_3 nanostructures with uniform dimensions. Furthermore, a plausible mechanism for the synthesis of θ-Al_2O_3 nanowires has been proposed, which is correlated with gross structural analysis as well as microstructural analysis. Moreover, the spectroscopic studies reveal that the estimated optical band gap of the material is 5.16 eV. The PL spectrum shows the blue emission to be peaking at 397 nm upon excitation at a wavelength of 252 nm. Time-resolved spectroscopic analysis suggests that the decay time of nanoseconds promises its suitability for many fast optical sensor applications.

Acknowledgements

We thank the Director, NPL New Delhi, India for providing the necessary experimental facilities. Dr Ajay Dhar, Dr S. N. Sharma, Mr J. S. Tawale and Dr R. Srivastava are gratefully acknowledged for providing the necessary instrumentation facilities for the XRD, FTIR, SEM and UV-vis spectroscopy, respectively. J. Gangwar acknowledges the financial support from UGC (grant no. F.2-61/98 (SA-I)).

Notes and references

1 X. S. Peng, L. D. Zhang, G. W. Meng, X. F. Wang, Y. W. Wang, C. Z. Wang and G. S. Wu, *J. Phys. Chem. B*, 2002, **106**, 11163.
2 J. Yoo, X. Ma, W. Tang and G. C. Yi, *Nano Lett.*, 2013, **13**, 2134.
3 A. Santos, G. Macías, J. F. Borrull, J. Pallarès and L. F. Marsal, *ACS Appl. Mater. Interfaces*, 2012, **4**, 3584.
4 H. Li, Y. Li, J. Jiao and H. M. Hu, *Nat. Nanotechnol.*, 2011, **6**, 645.
5 C. Barth and M. Reichling, *Nature*, 2001, **414**, 54.
6 X. S. Fang, C. H. Ye, X. X. Xu, T. Xie, Y. C. Wu and L. D. Zhang, *J. Phys.: Condens. Matter*, 2004, **16**, 4157.
7 I. J. Park, H. S. Roh, H. J. Song, D. H. Kim, J. S. Kim, W. M. Seong, D. W. Kim and K. S. Hong, *CrystEngComm*, 2013, **15**, 4797.
8 H. T. Chen, S. J. Xiong, X. L. Wu, J. Zhu and J. C. Shen, *Nano Lett.*, 2009, **9**, 1926.
9 C. Hou, Y. Xie, Q. Yang, Q. Guo and C. Tan, *Nanotechnology*, 2005, **16**, 741.
10 J. V. Foreman, J. Li, H. Peng, S. Choi, H. O. Everitt and J. Liu, *Nano Lett.*, 2006, **6**, 1126.
11 X. S. Fang, C. H. Ye, X. S. Peng, Y. H. Wang, Y. C. Wu and L. D. Zhang, *J. Mater. Chem.*, 2003, **13**, 3040.
12 A. Anjiki and T. Uchino, *J. Phys. Chem. C*, 2012, **116**, 15747.
13 X. Wu, S. Xiong, J. Guo, L. Wang, C. Hua, Y. Hou and P. K. Chu, *J. Phys. Chem. C*, 2012, **116**, 2356.
14 Y. Zhao, K. Kita, K. Kyuno and A. Toriumi, *Appl. Phys. Lett.*, 2009, **94**, 042901.
15 Z. Gu, F. Liu, J. Y. Howe, M. P. Paranthaman and Z. Pan, *Nanoscale*, 2009, **1**, 347.
16 M. D. Yang, K. W. Chen, J. L. Shen, J. C. Wang and C. Hsu, *Nanotechnology*, 2007, **18**, 405707.
17 M. Itou, A. Fujiwara and T. Uchino, *J. Phys. Chem. C*, 2009, **113**, 20949.
18 J. Lian, J. Ma, X. Duan, T. Kim, H. Li and W. Zheng, *Chem. Commun.*, 2010, **46**, 2650.
19 J. Yu, J. Wang, Z. Li, L. Li, Q. Liu, M. Zhang and L. Liu, *Cryst. Growth Des.*, 2012, **12**, 2872.
20 J. Gangwar, K. K. Dey, Komal, Praveen, S. K. Tripathi and A. K. Srivastava, *Adv. Mater. Lett.*, 2011, **2**, 402.
21 W. Cai, Y. Hu, J. Chen, G. Zhang and T. Xia, *CrystEngComm*, 2012, **14**, 972.
22 V. K. Das, R. R. Devi, P. K. Raul and A. J. Thakur, *Green Chem.*, 2012, **14**, 847.
23 M. B. I. Chowdhury, R. Sui, R. A. Lucky and P. A. Charpentier, *Langmuir*, 2010, **26**, 2707.
24 T. Kim, J. Lian, J. Ma, X. Duan and W. Zheng, *Cryst. Growth Des.*, 2010, **10**, 2928.
25 X. Y. Chen, Z. J. Zhang, X. L. Li and S. W. Lee, *Solid State Commun.*, 2008, **145**, 368.
26 S. Wang, A. Y. Borisevich, S. N. Rashkeev, M. V. Glazoff, K. Sohlberg, S. J. Pennycook and S. T. Pantelides, *Nat. Mater.*, 2004, **3**, 143.
27 C. K. Lee, E. Cho, H. S. Lee, K. S. Seol and S. Han, *Phys. Rev. B: Condens. Matter*, 2007, **76**, 245110.
28 E. N. Gribov, O. Zavorotynska, G. Agostini, J. G. Vitillo, G. Ricchiardi, G. Spoto and A. Zecchina, *Phys. Chem. Chem. Phys.*, 2010, **12**, 6474.
29 J. Choi, S. Zhang and J. M. Hill, *Catal. Sci. Technol.*, 2012, **2**, 179.
30 Z. Lodziana, N. Y. Topsoe and J. K. Norskov, *Nat. Mater.*, 2004, **3**, 289.
31 M. Kuramada, C. Koike and C. Kaito, *Mon. Not. R. Astron. Soc.*, 2005, **359**, 643.
32 Y. Xue, J. Lin, Y. Fan, J. Li, A. Elsanousi, X. Xu, D. Liu, Y. Huang, L. Hu, Y. Liu, F. Meng, J. Zou and C. Tang, *J. Cryst. Growth*, 2013, **382**, 52.
33 J. F. Lin, O. Degtyareva, C. T. Prewitt, P. Dera, N. Sata, E. Gregoryanz, H. K. Mao and R. J. Hemley, *Nat. Mater.*, 2004, **3**, 389.
34 G. Paglia, E. S. Božin and S. J. L. Billinge, *Chem. Mater.*, 2006, **18**, 3242.
35 G. Natu, Z. Huang, Z. Ji and Y. Wu, *Langmuir*, 2012, **28**, 950.
36 T. Li, S. Yang and Y. Du, *Nanotechnology*, 2005, **16**, 365.
37 N. F. Wu, H. J. Chen, Y. L. Chueh, S. J. Lin, L. J. Chou and W. K. Hsu, *Chem. Commun.*, 2005, 204.
38 M. K. Naskar, *J. Am. Ceram. Soc.*, 2009, **92**, 2392.
39 H. S. Roh, G. K. Choi, J. S. An, C. M. Cho, D. H. Kim, I. J. Park, T. H. Noh, D. W. Kim and K. S. Hong, *Dalton Trans.*, 2011, **40**, 6901.
40 C. C. Chang, J. L. Wu, N. H. Yang, S. J. Lin and S. Y. Chang, *CrystEngComm*, 2012, **14**, 1117.
41 P. Yan, G. T. Fei, G. L. Shang, B. Wu and L. D. Zhang, *J. Mater. Chem. C*, 2013, **1**, 1659.
42 X. Krokidis, P. Raybaud, A. E. Gobichon, B. Rebours, P. Euzen and H. Toulhoat, *J. Phys. Chem. B*, 2001, **105**, 5121.
43 Y. T. Pang, G. W. Meng, L. D. Zhang, W. J. Shan, C. Zhang, X. Y. Gao, A. W. Zhao and Y. Q. Mao, *J. Solid State Electrochem.*, 2003, **7**, 344.
44 X. Wang and Y. Li, *Inorg. Chem.*, 2006, **45**, 7522.
45 Q. Zhao, X. Xu, H. Zhang, Y. Chen, J. Xu and D. Yu, *Appl. Phys. A*, 2004, **79**, 1721.
46 S. Shen, W. K. Ng, L. S. O. Chia, Y. C. Dong and R. B. H. Tan, *Cryst. Growth Des.*, 2012, **12**, 4987.
47 S. C. Shen, W. K. Ng, Z. Y. Zhong, Y. C. Dong, L. Chia and R. B. H. Tan, *J. Am. Ceram. Soc.*, 2009, **92**, 1311.
48 M. Ma, Y. Zhu, G. Cheng and Y. Huang, *J. Mater. Sci. Technol.*, 2008, **24**, 637.
49 G. L. Teoh and K. Y. Liew, *J. Sol-Gel Sci. Technol.*, 2007, **44**, 177.
50 S. C. Shen, Q. Chen, P. S. Chow, G. H. Tan, X. T. Zeng, Z. Wang and R. B. H. Tan, *J. Phys. Chem. C*, 2007, **111**, 700.
51 C. C. Wang, C. C. Kei, Y. W. Yu and T. P. Perng, *Nano Lett.*, 2007, **7**, 1566.
52 C. Li, H. Huang, S. Yang, R. Zheng, W. Yang, Z. Liu and S. Ringer, *Mater. Lett.*, 2009, **63**, 1016.

53 I. Matolínová, S. Nemšák, M. Cabala, N. Tsud, J. P. Vejpravová, K. Veltruská, M. Yoshitake and V. Matolín, *J. Am. Ceram. Soc.*, 2011, **94**, 4084.
54 Y. Deng, Q. Yang, G. Lu and W. Hu, *Ceram. Int.*, 2010, **36**, 1773.
55 Q. Yang, *Bull. Mater. Sci.*, 2011, **34**, 239.
56 S. Banerjee, S. Maity and A. Datta, *J. Phys. Chem. C*, 2011, **115**, 22804.
57 A. L. M. Reddy, B. K. Gupta, T. N. Narayanan, A. A. Martí, P. M. Ajayan and G. C. Walker, *J. Phys. Chem. C*, 2012, **116**, 12803.
58 Z. Q. Yu, D. Chang, C. Li, N. Zhang, Y. Y. Feng and Y. Y. Dai, *J. Mater. Res.*, 2001, **16**, 1890.
59 V. A. Pustovarov and V. S. Kortov, *Tech. Phys. Lett.*, 2012, **38**, 511.
60 R. Toshima, H. Miyamaru, J. Asahara, T. Murasawa and A. Takahashi, *J. Nucl. Sci. Technol.*, 2002, **39**, 15.
61 Z. Q. Yua, C. X. Wanga, X. T. Gu and C. Li, *J. Lumin.*, 2004, **106**, 153.
62 S. Ikeda and T. Uchino, *J. Phys. Chem. C*, 2014, **118**, 4346.
63 C. W. Lowry, H. M. Gibbs, R. M. Pon and G. Khitrova, *Appl. Phys. Lett.*, 1990, **57**, 2759.